Modeling and Simulation of Capillary Microfluidic Networks Based on Electrical Analogies

Seok-Won Kang

Debjyoti Banerjee
e-mail: dbanerjee@tamu.edu

Department of Mechanical Engineering,
Texas A&M University,
College Station, TX 77843-3123

In this study we implemented the network simulation techniques using macromodels (lumped models) for capillary driven flows in microfluidic networks. The flow characteristics in a flow junction, such as meniscus stretching and bifurcation, were studied and their effects on filling time as well as pressure drop were explored for various network configurations. The results from the network simulator are validated numerically using computational fluid dynamics (CFD) simulations by employing the volume-of-fluids (VOF) method. The predictions by the network simulator for free-surface flows in different microfluidic networks were found to be in good agreement with the results obtained from the VOF simulations for filling time and meniscus position. [DOI: 10.1115/1.4004092]

1 Introduction

In capillary microchannels the surface effects (surface tension, contact angle, surface roughness ratio, etc.) dominate the bulk effects—as the volume of the fluid decreases and the surface/volume ratio increases with the progressive decrease in dimensions of the flow conduits. Accordingly, pressure drop in a capillary microchannel depends only on the viscous forces (major pressure head loss) [1] while minor pressure head losses become negligible since the inertial effects disappear. Typically, for devices involving capillary driven flows, the device operation is simulated using computational fluid dynamics (CFD) tools such as the volume-of-fluids (VOF) method or the level-set (LS) method.

Macromodels (also called "reduced-order model," "lumped parameter models," etc.) use a different approach to solving nonlinear and coupled problems by implementing behavioral subunits that are interlinked in a network model based on electrical analogies of resistance, capacitance, inductance, and logic units [2–5]. Macromodels enable the system level description based on behavioral representation of components that enable the solution of systems of linear differential equations or algebraic equations (in contrast, CFD techniques that are based on VOF and LS methods require the solution of discretized partial differential equations that are nonlinear and highly coupled. These numerical methods are typically used to solve the Navier–Stokes equations [6]. In addition, macromodels typically (1) are numerically simple, (2) are computationally simple (systems of ordinary differential equations or algebraic equations, as mentioned earlier), (3) are easy to implement (can be implemented in spreadsheet tools or mathematical solvers such as Matlab®, Mathematica®, or Simulink®), (4) are numerically robust; and (5) provide quick convergence to

the required solution (typically in fractions of seconds to a few minutes). Macromodel based solvers therefore enable fast design iterations and allow the users to rapidly traverse the design space. Hence macromodel based techniques serve as efficient design tools—especially for design situations where the underlying physics is not well understood or characterized but can still be amenable through the use of behavioral descriptions.

The primary drawbacks of the macromodels are that they are based on behavioral models and are not based on actual physical models. Hence the final configurations designed using macromodels are recommended for design verification using CFD tools or by experimental validations using actual prototypes before commencement of manufacturing and testing.

Several studies have been reported in the literature for the analyses and simulation of capillary driven flows in a single microchannel or microchamber [5,7–13]. However, the use of macromodels for free-surface flows involving the tracking of meniscus positions and capillary filling of microchannels/microchambers does not exist in the microfluidics literature for branched network configurations. Such problems always involve unsteady multiphase flows and the physical models for the appropriate representation of flow elements are often lacking.

In this study a methodology is presented for the lumped-parameter representation of free-surface flows in microfluidics. The emphasis of the study is on the effect of capillary bifurcations at junctions on the flow rate (meniscus propagation rates) in the different legs of the microfluidic networks architectures, filling time and pressure drop as a function of the viscosity, surface tension, and contact angles at different locations of the network. The macromodel is implemented in a graphic user interface (GUI) using Matlab® solver and the accuracy of the predictions are verified by performing VOF simulations using a commercial CFD tool (Fluent®).

2 Analysis of Capillary Driven Flows

In a capillary microchannel the longitudinal component of the surface tension force at the free surface must balance the pressure drop due to viscous force in the conduits upstream from the location of the meniscus [5].

$$\Delta p = \frac{4\sigma \cos\theta}{D_h} = f_D \frac{L}{D_h} \frac{\rho u^2}{2} \qquad (1)$$

For laminar flow in rectangular cross section of aspect ratio 1, $f_D \mathrm{Re}_{D_h}$ is 56.91 [6]. The electrical analogies of this microfluidic system are listed in Table 1.

From Eq. (1) and the values of $f_D \mathrm{Re}_{D_h}$ in a straight square (aspect ratio = 1) shaped capillary microchannel, the circuit representation in the electrical domain is given by the following expression:

$$\Delta p = \frac{28.455\mu}{D_h^2} L \cdot u = \frac{28.455\mu}{D_h^4} L \cdot \phi = R \cdot i = e \qquad (2)$$

Equation (1) is a specific form of the Lucas and Washburn equation [14,15]. This equation has been modified and applied in several forms for different flow conditions by changing the boundary and initial conditions [14–19]. The Lucas and Washburn equations have also been investigated using noncontinuum based models using molecular dynamics (MD) techniques [20].

Capacitance effects arise from compressibility of the flow. In these analyses incompressible flow equations have been used and therefore capacitance issues have not been considered in this study. The inertance effect arises from the volume of the mass of the fluid and fast acceleration of the fluid. Such effects are more pronounced in the initial phases of liquid entry into the microchannels [15–19]. However, for branched channel flows considered in this study the reduction in flow rates at the junctions will further reduce the magnitude of the corrections required to adjust

Table 1 Microfluidic simulation variables and their electrical analogies

Microfluidic system		Electrical system	
φ or (u)	Volumetric flow rate (velocity)	i	Current
p	Pressure	e	Voltage
$\frac{f_D}{2}\mu L/A^2$; $\left(\frac{f_D}{2}\mu L/A\right)$[a]	(where f_D is the Darcy friction factor)	R	Resistance

[a] A is the area normal to the direction of fluid motion.

for the inertance effects. Hence inertance effects have not been considered in this study.

3 Numerical Models

Volume-of-fluids (VOF) method is typically used to simulate the meniscus position during multiphase flows in microchannels [7]. The Navier–Stokes equations in the VOF model are discretized using second order schemes with the second order up-winding method. The segregated solver is applied with the PISO pressure correction method. The 3D model involving a square cross section is generated in Gambit®. A pressure inlet boundary condition is applied with a small gauge pressure of 20 Pa to enable faster numerical convergence (this result is expected to be almost identical to that of 0 gauge pressure for the microchannel geometries, but a small inlet pressure helps with faster numerical convergence and with less propensity for numerical oscillations).

Figure 1(a) depicts the geometry of a representative microchannel network with a square shaped artery microchannel (hydraulic diameter D_{mh}) and three tributary tubes with a rectangular cross section (hydraulic diameter D_{Th}) where the horizontal pitch for the tributary microchannels is L_i and the length of the tributary microchannels is l_T. The length of the liquid column at any instant in the region between two tributary columns is denoted by L_i. The boundary conditions imposed were (1) pressure inlet boundary condition at the entrance of the artery microchannel and (2) outlet boundary condition at the end of the tributary microchannels. The initial length of the artery is L_0 and the length of liquid column at any instant of time in each tributary (i) is denoted by L_{Ti}. Simulations in the macromodel are started by assuming a value for the initial liquid column in the artery and setting the values of L_{Ti} to zero.

The corresponding electrical network representing the time-dependent resistances for each leg of the network (which would vary as a function of the transient location of the menisci) is shown in Fig. 1(b). The potential source (pressure source) due to the capillary pressure at the location of the menisci in each segment of the artery microchannel and the tributary microchannel are shown in the figure. The pressure source at the inlet is also represented in this network diagram.

The bifurcations of the menisci at the flow junctions represent a particular challenge for formulating the macromodel equations. If the grid generation schemes are not optimized for this meniscus stretching and folding during flow bifurcations at the T junctions, considerable numerical oscillations can be generated, resulting in erroneous predictions for flow resistances as well as filling times. The solvers are prone to such numerical oscillations as the flow dimensions are reduced and are particularly severe when the diameter ratios between the artery and tributaries are of the order of unity (i.e., $D_{mh}/D_{Th} \approx 1$) and the ratio of tributary pitch to the tributary diameter is of the order of unity (i.e., $L_i/D_{mh} \approx 1$). If the meniscus at the previous junction does not bifurcate fully before the meniscus reaches the next flow junction, nonlinear feedback interactions can occur between the flows in the different tributaries, thus making the lumped parameter (flow-resistance) models invalid. This type of nonlinear interactions between two different tributary channels can also occur for several combinations of: diameter ratios (D_{mh}/D_{Th}), tributary diameter-to-length ratios (D_{Th}/l_T), tributary length-to-pitch ratios (l_T/L_i), and tributary diameter-to-pitch ratios (L_i/D_{Th}). For example, the pitch L_i should be larger than the length of the tributary channel, for contact angles less than 45°. An exploration of these parameters on the applicability of the system models is not the focus of this study; however, these limitations are prerequisites for the validity of system models.
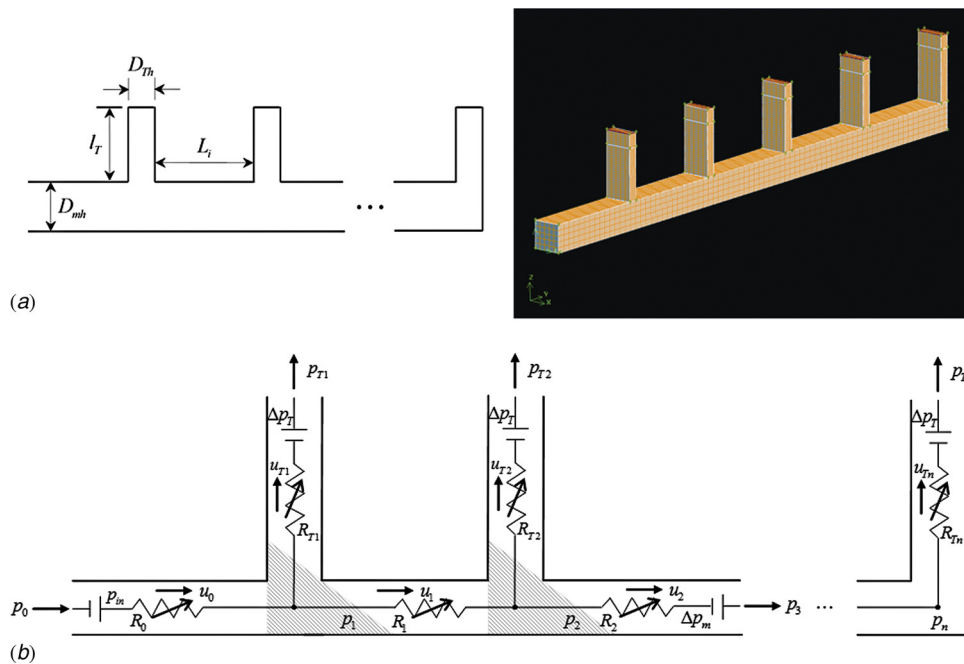

Fig. 1 (a) (Top) Schematic and (bottom) solid model of the flow geometry of the capillary microfluidic network. (b) Equivalent system model for filling of the microfluidic network is represented by time-dependent resistor elements and potential sources.

4 System Model

4.1 Lumped Parameter Model Formulation. Figure 1(*b*) represents the equivalent network model for a microfluidic network distributing the capillary driven flow from the main artery microchannel into the tributaries. The system model was based on the principle of electrical networks (Kirchhoff's voltage law: KVL) and the concept of *R-L-C* device models, which was then applied to the microfluidic devices.

The pressure drop is considered to be time dependent where the value of each flow resistance is also time dependent and is governed by the time-dependent position of menisci in each leg of the network. The value of the resistance (R) is a function of the liquid column in each leg of the network and is described by Eq. (1). From the analogies given in Table 1 the flow resistance values are given by

$$R_0 = \frac{28.455\mu}{D_m^2}L_0 \tag{3}$$

$$R_i = \frac{28.455\mu}{D_m^2}L_i \tag{4}$$

$$R_{Ti} = \frac{28.455\mu}{D_T^2}L_{Ti} \tag{5}$$

and the flow resistances in each tributary (or leg of the artery) depend on the respective length of the liquid column. As mentioned before, estimating the flow resistance for the junctions in meniscus driven flows is tricky due to effects of meniscus stretching and folding which affect the values of the dynamic contact angles. In particular, based on flow conservation, at each T junction depicted as the shaded region in Fig. 1(*b*), the incoming flow in the junction region must be balanced by the total outflow into the downstream segment of the main channel and the tributary channels. For an explicit scheme involving a time interval Δt, this can be expressed mathematically as

$$\rho A u_0 \Delta t = \rho A L_i + \rho A_T L_{Ti} \tag{6}$$

Also assuming the pressure drop is balanced between the downstream segments at the junction of the artery and tributary, the flow is split between the two branches in a geometric ratio using Eqs. (1), (2), (4), and (5) as follows:

$$\frac{L_{Ti}^2}{D_T^2} = \frac{L_i^2}{D_m^2} \tag{7}$$

The capillary pressure due to meniscus position in the artery and tributary are denoted as Δp_m and Δp_T are given by

$$\Delta p_m = \frac{4\sigma \cos\theta}{D_m} \tag{8}$$

$$\Delta p_T = \frac{4\sigma \cos\theta}{D_T} \tag{9}$$

The pressure drop in microchannels can be treated as the voltage drop between two nodes. The flow equations in the microfluidic network shown in Fig. 1(*b*) can be represented as the linear simultaneous equations as follows:

$$R_0 u_0 + \sum_{i=1}^{n-1} R_i u_i = p_{in} + \Delta p_m \tag{10}$$

$$\sum_{i=0}^{j-1} R_i u_i + R_{Tj} u_{Tj} = p_{in} + \Delta p_T \text{ for } j = 1, 2, \ldots, n-1 \tag{11}$$

$$A u_i - A_T u_{Ti+1} - A u_{i+1} = 0 \text{ for } i = 0, 1, \ldots, n-2 \tag{12}$$

$$A u_{n-1} - A_T u_{Tn} = 0 \tag{13}$$

For the final (*n*th) channel, Eq. (14) as well as Eqs. (11)–(13) should be employed instead of Eq. (10).

$$R_0 u_0 + \sum_{i=1}^{n-1} R_i u_i + R_{Tn} u_{Tn} = p_{in} + \Delta p_T \tag{14}$$

where A and A_T are cross section area of capillary. The linear set of equations given by Eqs. (10)–(13) (or Eq. (14)) are solved at a given time step (*n*) for the unknown values of u_i and u_{Ti} by substituting the time-dependent flow resistance values from Eqs. (3)–(5). Finally, the location of the meniscus at each time step $(n + l)$ is obtained from the location in the previous time step (*n*) using a explicit scheme as follows:

$$L_i^{n+1} = L_i^n + u_i^{n+1} \Delta t \tag{15}$$

$$L_{Ti}^{n+1} = L_{Ti}^n + u_{Ti}^{n+1} \Delta t \tag{16}$$

4.2 Effect of Dynamic Contact Angle on Meniscus Displacement at T Junction. The flow redistribution in the junctions causes meniscus stretching, folding, and additional free-surface generation (topological change) which would result in additional flow resistances and impede the propagation rates of the menisci. The stretching of meniscus at the capillary junctions causes the retardation of flow [7]. However, implementing the geometrical effects arising from the variation of the wetting perimeter in the conduit junctions into the lumped parameter model is cumbersome and such variations in physical behavior are difficult to predict. Nevertheless, the variation of dynamic contact angle at the flow junctions need to be incorporated into the macromodels since there is a significant retardation of the propagation rates due to the meniscus bifurcation which also affects the resulting filling time.

The dynamic behaviors of contact angle for partially wetted surfaces are known to vary drastically based on flow regimes defined by the capillary number ($Ca = \mu\, U/\sigma$) [8,9]. The relationship between contact angle and capillary number is based on Kistler's model [8,9]. For the flow regimes based on the range of capillary numbers used in the lumped models in this study, the dynamic contact angles have higher values than (static) equilibrium value of 10°. In addition, the meniscus stretches downstream into the artery microchannel from the capillary junction area even before the meniscus has completely bifurcated into the two microchannels at the T junction. Thus the meniscus bifurcation process results in an enhancement the effective length of the microchannels, both on the artery and tributary side downstream of the junction. This enhancement of the effective length can be incorporated in the macromodel by considering the junction volume (as shown in Eqs. (6) and (7)) and by specifying an effective dynamic contact angle (which will be higher than the static contact angle).

5 Results and Discussion

Simulations were performed using the macromodel for single microchannels that are 3 μm in length with square shaped cross sections by specifying various hydraulic diameters and for properties of water. In these simulations for various values of hydraulic diameters are used: 200, 300, 400, and 500 nm. The purpose of this exercise was to validate the macromodel predictions using results obtained from VOF simulations. Using Eqs. (1) and (2) the expression for the filling time (τ) for a single microchannel is obtained as [6]

$$\left(\frac{16\sigma\cos\theta}{f_D \mu D_h}\right)\tau = \frac{L_2^2 - L_1^2}{D_h^2} \tag{17}$$

Figure 2 shows the results for the filling time for the different hydraulic diameters obtained from the simulations using the VOF
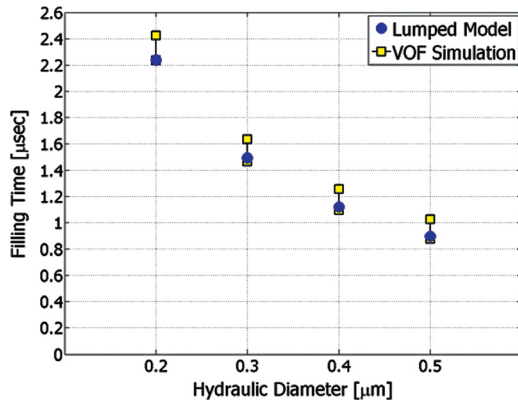
Fig. 2 Comparison of results obtained from macromodel and VOF method for filling time as a function of hydraulic diameter for a single micro-channel

Table 2 Geometric parameters used in VOF simulation

	D_{mh} (μm)	D_{Th} (μm)	d (μm)	l_T (μm)	$f_D Re_{D_h}$
Case A	0.4	0.2	1.5	0.75	68.83
Case B	0.4	0.2	1.5	0.75	56.91
Case C	4.0	2.0	15.0	7.5	68.83
Case D	4.0	2.0	15.0	7.5	56.91

model and the macromodel. For the VOF model two values of the filling time are shown for each hydraulic diameter. The lower value of filling time corresponds to the time of arrival of the edge of the meniscus at the outlet of the microchannel, while the higher value of the filling time corresponds to the center of the meniscus reaching the outlet of the microchannel. The predictions from the macromodel Eq. (17) are observed to be in good agreement with the VOF results and consistently matches the lower value of the filling time obtained from the VOF model.

The next step in the numerical validation was to apply the macromodel for a microfluidic network architecture involving an artery microchannel and an array of tributary microchannels of different hydraulic diameter. Figure 3 shows the meniscus position as a function of time in the artery and tributary microchannels that are obtained from the macromodel and the VOF simulations. The location of the meniscus for filling of microchannels is plotted at regular time intervals (Δt). The simulations were performed for the fluid thermophysical properties of water, where viscosity is $\mu = 0.001003$ kg/m s, density is $\rho = 998.2$ kg/m^3, surface tension is $\sigma = 0.0728$ N/m, and contact angle is $\theta = 10°$. The geometric design parameters for the four cases that were used in the VOF simulations and macromodel (system model) are summarized in Table 2. The simulations were performed for rectangular and square geometries where the hydraulic diameters, the channel lengths, and the pitch of the tributary microchannels were scaled by a factor of 10 for both cases.

The line plotted in pink color in Fig. 3 shows the predictions from the macromodel for a single microchannel (with no tributaries) of the same length and hydraulic diameter as the artery microchannel. This plot gives an estimate for the reduction in filling time due to flow into the tributary microchannels (which provide additional capillary pumping sources as well as additional
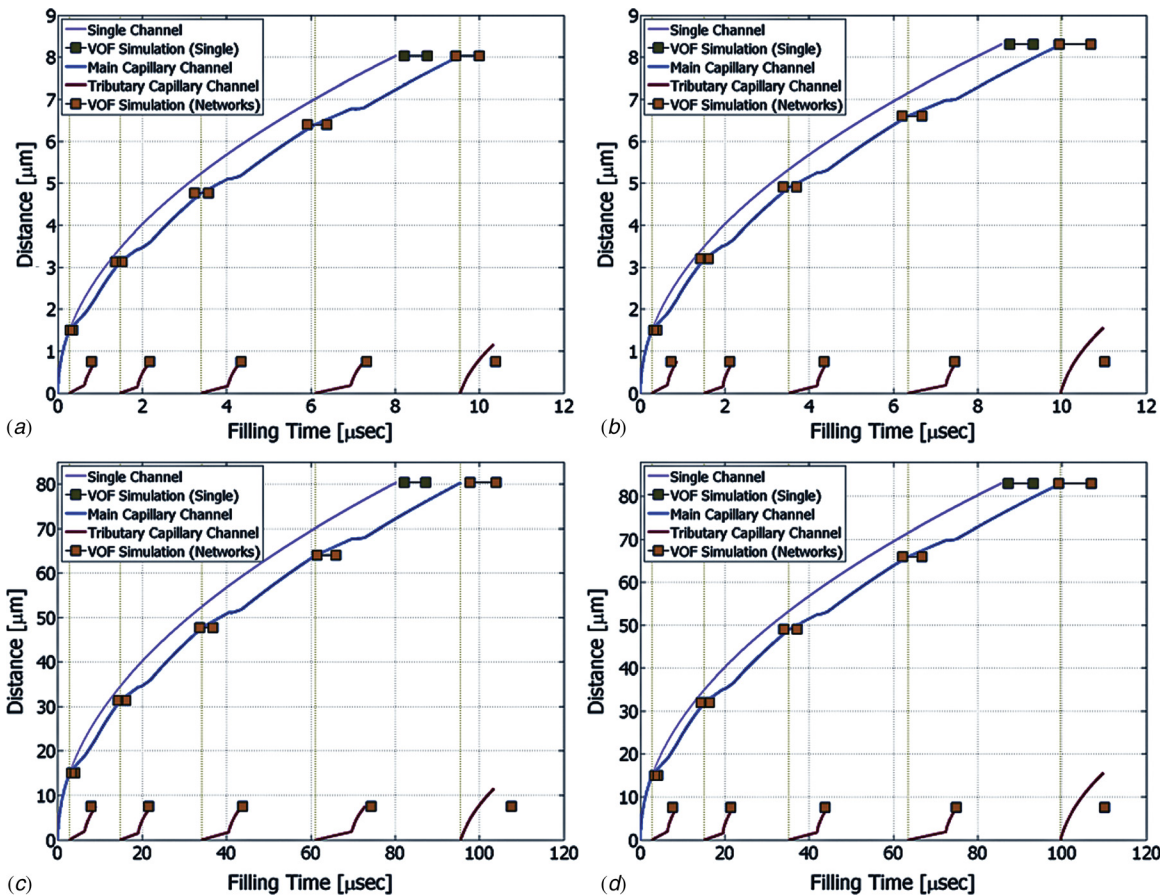

Fig. 3 Comparison of meniscus position and filling time for macromodel and VOF simulation for contact angle of 10°

resistance to capillary driven flow). The VOF simulation corresponding to a single microchannel (with no tributaries) of the same length and hydraulic diameter as the artery microchannel is plotted using a pair of green markers in the same plots. One of the markers represents the lower value of filling time for the edge of the meniscus and the other marker represents the higher value of filling time corresponding to the midsection of the meniscus.

The actual value of the meniscus position in the artery microchannel obtained from the macromodel is plotted using a blue line. The actual value of the meniscus position in the artery microchannel obtained from the VOF simulations is plotted using two yellow markers to show the range of filling times associated with the edge of the meniscus and the midplane of the meniscus. The meniscus position in the tributary microchannels is plotted using a red line for the macromodel solutions. The meniscus position in the tributary microchannels is plotted using a single yellow marker for the VOF simulations corresponding to the edge of the meniscus.

The plots in Fig. 3 for the four cases A, B, C, and D of Table 2 show that the macromodel is in good agreement for the filling time for the artery microchannel at the junction locations, underpredicting the results from the VOF simulations by less than ~5% at the third and fourth junctions. The filling time for the artery microchannel is underpredicted by the macromodel by less than 9%, compared to the results obtained from the VOF simulation.

The meniscus propagation rate is shown to be at a reduced rate in the artery microchannel during the duration of meniscus formation in the junctions as well as the formation and propagation of additional free surfaces in the tributary microchannels. This is demonstrated by a reduction in the slope of the meniscus position as a function of time. This is to be expected since the filling of tributary microchannels represents a leakage in the flow from the artery. The creation of additional menisci also results in additional resistances to flow. However, in the intervening period after a tributary channel is filled and before the next flow junction is reached, the meniscus propagation rate in the artery microchannel is found to be similar to the single microchannel results (the two curves, blue and pink, are found to be approximately parallel and have similar parabolic shapes, as would be expected from Eq. (17)).

The meniscus motion in the tributary channel is found to have a linear variation in the initial phase of the filling. This linear filling rate is an artifact of the behavioral approximation of meniscus stretching represented by Eqs. (6) and (7). In reality the meniscus stretching, folding, and the subsequent generation of an additional meniscus in the tributary microchannel due to flow bifurcation from the artery microchannel will cause even slower filling rate than shown in Fig. 3. After the flow bifurcation is accomplished and the meniscus in the tributary microchannel propagates towards the exit plane. At this stage the filling rate (or meniscus propagation rate) is expected to have a parabolic profile in accordance with Eq. (17). Thus the filling time of the first and second tributary microchannels predicted by the macromodel is found to be in good agreement with the VOF simulation results. The macromodel underpredicts the filling time for the third and fourth tributary by less than 5%. The filling time for the fifth tributary is under predicted by less than 9% by the macromodel when compared to the corresponding VOF simulation results.

According to the numerical and experimental validation of Saha and Mitra [9], although the dynamic contact angle has marginal effect on the capillary flow, it significantly affects the displacement rates of menisci. As mentioned before, the effect of the meniscus stretching, junction volume, and junction resistance can be accounted for by using a higher value of the effective contact angle. By progressively increasing the user specified value of the contact angle to $25°$ in the macromodel, it was found that the macromodel results (for meniscus positions in the third, fourth, and fifth junction as well as tributary filling time) are in better agreement with the VOF results for static contact angle of $10°$.

6 Summary and Conclusions

Macromodels based on electrical analogies are derived for capillary driven microfluidic networks. Macromodel predictions for single microchannel architectures are in good agreement with results obtained from VOF simulations. For microfluidic networks the bifurcation of meniscus at flow junctions can cause significant stretching and folding of menisci, which can tax the total flow energy budget, thereby causing significant retardation of the meniscus propagation in the artery microchannel as well as tributary microchannels. These effects are incorporated into the macromodel used in this study and the predictions from the macromodel therefore underpredict the VOF simulation results by less than 10%.

Nomenclature

Ca = capillary number
D_h = hydraulic diameter (m)
d_{eff} = effective length added to length of microchannels at a junction (m)
d_j = meniscus position in microchannel junction (m)
e = analogous flow potential drop (N/m^2 or kg/m s^2)
f_D = Darcy friction factor (which is a function of geometrical parameters of the cross section)
i = analogous flow current (m^3/s)
L = length of the microchannel (m)
R = analogous flow resistance (kg/m^2 s)
Re_{D_h} = $\rho u D_h / \mu$, Reynolds number
u = mass averaged velocity (which is also the velocity of the meniscus in the microchannel) (m/s)
Δp = pressure drop (N/m^2 or kg/m s^2)
θ = contact angle (rad)
μ = kinematic viscosity of the working fluid (kg/m s)
ρ = density (kg/m^3)
σ = surface tension (N/m)
ϕ = volume flow rate (m^3/s)

References

[1] Jian, S., and Lin, M., 2006, "Effect of Smooth Microchannel Cross Section Shape on Friction Factor," *1st IEEE International Conference on Nano/Micro Engineered and Molecular Systems*, Zhuhai, China, Jan. 18–21.
[2] Banerjee, D., 2005, "Experimental Validation of Macromodels for Simulating Capillary Driven Multi-Phase Flows Used for Microchamber Filling," Proceedings of INTERPACK2005, The ASME/Pacific Rim Technical Conference and Exhibition on Integration and Packaging of MEMS, NEMS and Electronic Systems, San Francisco, CA, Jul. 17–22, INTERPACK2005-73412.
[3] Bourouina, T., and Grandchamp, J., 1996, "Modeling Micropumps with Electrical Equivalent Networks," *J. Micromech. Microeng.*, **6**, pp. 398–404.
[4] Chatterjee, A. N., and Aluru, N. R., 2005, "Combined Circuit/Device Modeling and Simulation of Integrated Microfluidic Systems," *J. Microelectromech. Syst.*, **14**(1), pp. 81–95.
[5] Banerjee, D., Amro, N. A., and Fragala, J., 2005, "Optimization of Microfluidic Ink-Delivery Apparatus for Dip Pen Nanolithography™," *SPIE J. Microlith., Microfab. and Microsyst*, **4**, pp. 023014–023021.
[6] White, F. M., 2003, *Fluid Mechanics*, McGraw-Hill, New York.
[7] Saha, A. A., and Mitra, S. K., 2008, *Recent Advances in Modeling and Simulation: Chap 17 Modeling and Simulation of Microscale Flow*, InTech Education and Publishing, Austria.
[8] Sikalo, S., Wilhelm, H. D., Roisman, I. V., Jakirlic, S., and Tropea, C., 2005, "Dynamic Contact Angle of Spreading Droplets: Experiments and Simulations," *Phys. Fluids*, **17**, pp. 062103.

[9] Saha, A. A., and Mitra, S. K., 2009, "Effect of Dynamic Contact Angle in a Volume of Fluid (VOF) Model for a Microfluidic Capillary Flow," J. Colloid Interface Sci., **339**, pp. 461–480.

[10] Banerjee, D., 2005, "Investigation of Volume of Fluids (VOF) Method and System Models for Design of Microfluidic Ink Delivery Apparatus for Dip Pen Nanolithography (DPN)," Nano Science and Technology Institute (NSTI) Nanotechnology 2005/NanoBio2005, Anaheim, CA, May 10–12, Vol. 1, pp. 680–683.

[11] Chakrabarty, K., and Zeng, J., 2005, "Design Automation for Microfluidics-Based Biochips," J. Emerging Technol. Comput. Syst., **1**(3), pp. 186–223.

[12] Wang, K.-L., and Jones, T. B., 2005, "Saturation Effects in Dynamic Electrowetting," Appl. Phys. Lett., **86**, pp. 054104.

[13] Saha, A. A., and Mitra, S. K., 2009, "Numerical Study of Capillary Flow in Microchannels with Alternate Hydrophilic-Hydrophobic Bottom Wall," ASME J. Fluids Eng., **131**(6), pp. 061202.

[14] Washburn, E. W., 1921, "The Dynamics of Capillary Flow," Phys. Rev., **27**(3), pp. 273–283.

[15] Lucas, V. R., 1918, "Uber das Zeitgesetz des Kapillaren Aufstiegs von Flussigkeiten," Kolloid. Zh., **23**, pp. 15–22.

[16] Hamaraoui, A., and Nylander, T., 2002, "Analytical Approach for the Lucas–Washburn Equation," J. Colloid Interface Sci., **250**, pp. 415–421.

[17] Zhmud1, B. V., Tiberg, F., and Hallstensson, K., 2000, "Dynamics of Capillary Rise," J. Colloid Interface Sci., **228**, pp. 263–269.

[18] Friesa, N., and Dreyer, M., 2008, "An Analytic Solution of Capillary Rise Restrained by Gravity," J. Colloid Interface Sci., **320**(1), pp. 259–263.

[19] Friesa, N., and Dreyer, M., 2008, "The Transition from Inertial to Viscous Flow in Capillary Rise," J. Colloid Interface Sci., **327**(1), pp. 125–128.

[20] Martic, G., Gentner, F., Seveno, D., Coulon, D., and Coninck, J. De, 2002, "A Molecular Dynamics Simulation of Capillary Imbibition," Langmuir, **18**, pp. 7971–7976.